ANNALS OF GEOPHYSICS, 68, 3, NS334, 2025; doi:10.4401/ag-9122
OPEN ACCESS

Modeling and advanced Ground Penetrating Radar techniques for evaluating pipe leakage and pavement distress

João Andrade dos Reis Júnior[1], Herson Oliveira da Rocha[*,2], Maykon Masao Yano Taniyama[1], Gildenilson Mendes Duarte[1], Diego da Costa Miranda[3], Francisco Pinheiro Lima-Filho[4]

(1) Federal Rural University of Amazônia (UFRA), Environmental, Geosciences, and Engineering Study Group (GEMAGE), Belém, Brazil
(2) Federal University of Rio de Janeiro (UFRJ), Polytechnical Institute (IPOLI), Macaé, Brazil
(3) Federal University of Pará (UFPA), Geoscience Institute (IG), Belém, Brazil
(4) Federal University of Rio Grande do Norte (UFRN), Postgraduate Program in Geodynamics and Geophysics (PPGG), Natal, Brazil

Article history: received July 10, 2024; accepted October 15, 2024

Abstract

This study provides a comprehensive analysis of Ground Penetrating Radar (GPR) data processing techniques for detecting water leakage in urban pavements. By examining GPR images characterized by continuous and discontinuous high-amplitude reflections, the research identifies clear indicators of water saturation caused by leaking underground pipes. Computer modeling of GPR profiles enables effective comparisons with real data and helps in calibrating key GPR attributes such as energy, amplitude variance, and RMS amplitude. These attributes allow for the precise delineation of leakage zones in both synthetic and real GPR datasets collected in the Amazon region of Brazil. The Reflector Tilt Method (RTM) significantly enhances GPR data analysis, especially for detecting subsurface water leaks. RTM utilizes changes in the relative dielectric constant and electromagnetic wave velocity induced by water saturation in unconsolidated, horizontally stratified sand layers. By analyzing the tilt of reflections in GPR profiles, RTM differentiates between dry and saturated zones, providing insights into the geometry and extent of water infiltration. Notably, this study demonstrates how increased subsurface water saturation causes underlying reflectors to tilt. Using the tilt angle, we propose a novel technique to quantify the increase in the dielectric constant due to water saturation. This technique could also be adapted to detect leaks involving other fluids, as long as there is a strong contrast between the dielectric constant and the background. The integration of RTM improves the creation of accurate three-dimensional models of affected areas, enhancing leak detection and aiding in understanding water movement dynamics within the subsurface. The study underscores the importance of combining GPR attributes with RTM to generate detailed 3D models of leakage zones, which are essential for estimating the volume of infiltrated areas. Observations indicate significant water saturation near leaking pipes at shallow depths, with saturation levels decreasing rapidly as depth increases. By identifying 2D geophysical signatures of water leaks in public distribution networks, the research highlights the effectiveness of non-invasive GPR methods in mitigating risks such as soil erosion and surface collapse. This approach demonstrates the utility of GPR attributes and RTM as essential tools for assessing urban pavement integrity, enabling early

detection of leaks and precise mapping of affected zones. The findings contribute significantly to the efficient and sustainable management of urban infrastructure, enhancing maintenance strategies and reducing potential hazards associated with undetected fluid leaks.

Keywords: Pavement Collapses; Pipeline Leaks; Ground Penetrating Radar; Subsurface Anomalies

1. Introduction

The main challenge in road infrastructure studies is to assess the quality of pavements in a practical, non-destructive, and cost-effective way. Information on layer thickness is crucial for pavement repair (De Souza Moreira et al., 2022). Urban pavements remain extremely precarious in certain regions worldwide, such as also in our study site in Brazil. It is known that a significant part of these problems are due to inadequate public administration, coupled with the employment of unskilled labor and the hiring of uncertified companies.

The issues affecting traffic flow, such as potholes, bumps, and other road irregularities, can largely be attributed to a set of pr evalent problems. This study identifies and discusses four key factors contributing to these challenges: (i) lack of technical studies and projects, (ii) basic execution failures, (iii) ayer overlapping, and (iv) excessive use of patches.

Traffic studies, subsoil investigations, and the correct sizing of layers using the Marshall method are examples of steps that need to be taken before asphalt mixes are applied to ensure that the material can be applied (Azarhoosh and Pouresmaeil, 2020). It is not enough to simply build over a base that appears to be ready for paving. The consequences of the lack of investment, studies and qualified technical planning increase the early deterioration that makes driving difficult and poses a danger to drivers and pedestrians.

Asphalt has a limited lifespan, with problems arising due to daily wear and tear and oxidation of petroleum asphalt cement (PAC), which reduces its elasticity (Khedaywi and Melhem, 2024; Zhang and Kevern, 2021). A common issue in urban pavements is the overlapping of layers, where new layers are applied without removing the old ones, leading to recurring depressions and further shortening the pavement's life. When signs of damage appear, a detailed investigation is advised. However, patching with cold asphalt, while useful for certain repairs, should not be overused. Multiple faults indicate that the current layer may need to be removed or a deeper intervention is necessary (Riviera et al., 2020).

Another challenge is the detection of underground leaks in urban pavements, as these usually do not provide signs on the surface. Underground leaks are often associated with diffuse flow through small cracks or damaged joints. This pattern is characterized by a rapid pressure drop that often cannot be detected by measuring instruments (Adedeji et al., 2017).

As direct observation is not possible, many cubic meters of water are lost unnoticed. This can also lead to soil erosion and, in severe cases, surface collapse in the affected area, resulting in pavement destruction and, in some cases, serious accidents. The detection of these leaks usually requires invasive techniques such as drilling, stress tests, or traffic simulations, which emphasizes the importance of non-destructive and cost-effective methods (Canestrari and Ingrassia, 2020; Hong et al., 2018; Neves et al., 2023).

There are several non-destructive methods for detecting leaks in urban pavements, such as ground motion sensors, ultrasonic wave testing, and ground penetrating radar (GPR) (Zang et al., 2023; Wang et al., 2021; Xiong et al., 2024). Of the methods mentioned, only GPR can image the subsurface with high resolution. This technique has proven to be successful in identifying the spatial location of pipes and sewer networks, determining the depth and extent (2D or 3D) of the area affected by leaks (wet zone), and detecting voids created by water flow disturbing the ground and carrying sediments. In addition, GPR enables significant advances in obtaining 3D images of water leakage under asphalt pavement (Luo et al., 2020; Tso et al., 2020; Raiol et al., 2019; Lai et al., 2018).

Ayala-Cabrera et al. (2014) examined the progression of water leakage detection methods based on GPR data, highlighting the evolution of techniques over time. De Coster et al. (2019) discussed advancements in GPR technology aimed at improving the detection of pipes and leaks within water distribution networks, focusing on both technological and methodological improvements. Lau et al. (2021) focused on the use of GPR wave velocity

algorithms to characterize and detect pipe leaks, offering a technical approach to analyzing GPR data. Liu et al. (2022) explored the signal characteristics of GPR in environments prone to groundwater pipe leakage, providing insights into effective signal interpretation for leak detection.

Yang et al. (2022) employed an innovative approach using electric field component imaging with GPR to detect anomalies, including leaks, in pipelines, offering a novel perspective on GPR applications. Gamal et al. (2023) demonstrated the practical application of GPR in detecting water leaks and characterizing pipe materials, emphasizing its utility in real-world environmental studies. Zhang et al. (2024) introduced an advanced method that combines GPR with image correlation algorithms, enhancing the precision of leak detection in water supply pipelines. Zhu et al. (2024) integrated hydromechanical modeling with electromagnetic modeling to improve the accuracy of GPR-based leak detection, providing a robust framework for future applications.

The present study aims to improve the detection of water leaks in a city in the Brazilian Amazon by using mathematical attributes in GPR data. The aim is to delineate the wet zone more accurately, including potentially eroded areas under the asphalt pavement. To achieve this, a case study will be conducted using a GPR data processing workflow that calibrates the attributes' parameters. The Reflection Tilt Method (RTM) is used in this innovative approach to create 3D models of the area affected by water pipe leaks.

2. Study Area

2.1 Geographic Location and Geological Setting

The Brazilian state of Pará is known for its vast territory (1,247,689 km^2) and extensive hydrographic network, particularly in the Amazon region. It is divided into three large hydrographic basins: The Amazon River basin, the basins of the Tocantins and Araguaia rivers, and that of the western Northeast Atlantic. Pará also includes the catchment area of the Caeté River, which covers a total area of 2,235.14 km^2.

This catchment drains parts of seven municipalities in Pará: Augusto Corrêa, Bonito, Bragança, Capanema, Ourém, Tracuateua and Santa Luzia do Pará. Table 1 shows the percentage share of each municipality in the catchment area and the share of the catchment area to each city.

In this context, the city of Capanema is considered one of the most developed cities in the north-eastern state of Pará (Fig. 1). However, there are still significant problems with the local infrastructure, including the lack of paved roads, sewage systems, and a reliable water supply.

Cities	Total Area (km^2)	Area in the basin (km^2)	City (%)	Basin (%)
Augusto Corrêa	1,091.541	24.57	2%	1%
Bonito	586.736	189.65	24%	8%
Bragança	2,091.930	1,169.85	36%	52%
Capanema	614.693	125.64	17%	6%
Ourém	562.388	125.65	18%	6%
Santa Luzia	1,356.124	475.63	26%	21%
Tracuateua	934.272	124.15	12%	6%

Table 1. Distribution of the area of the municipalities, belonging to the Caeté River Hydrographic Basin.

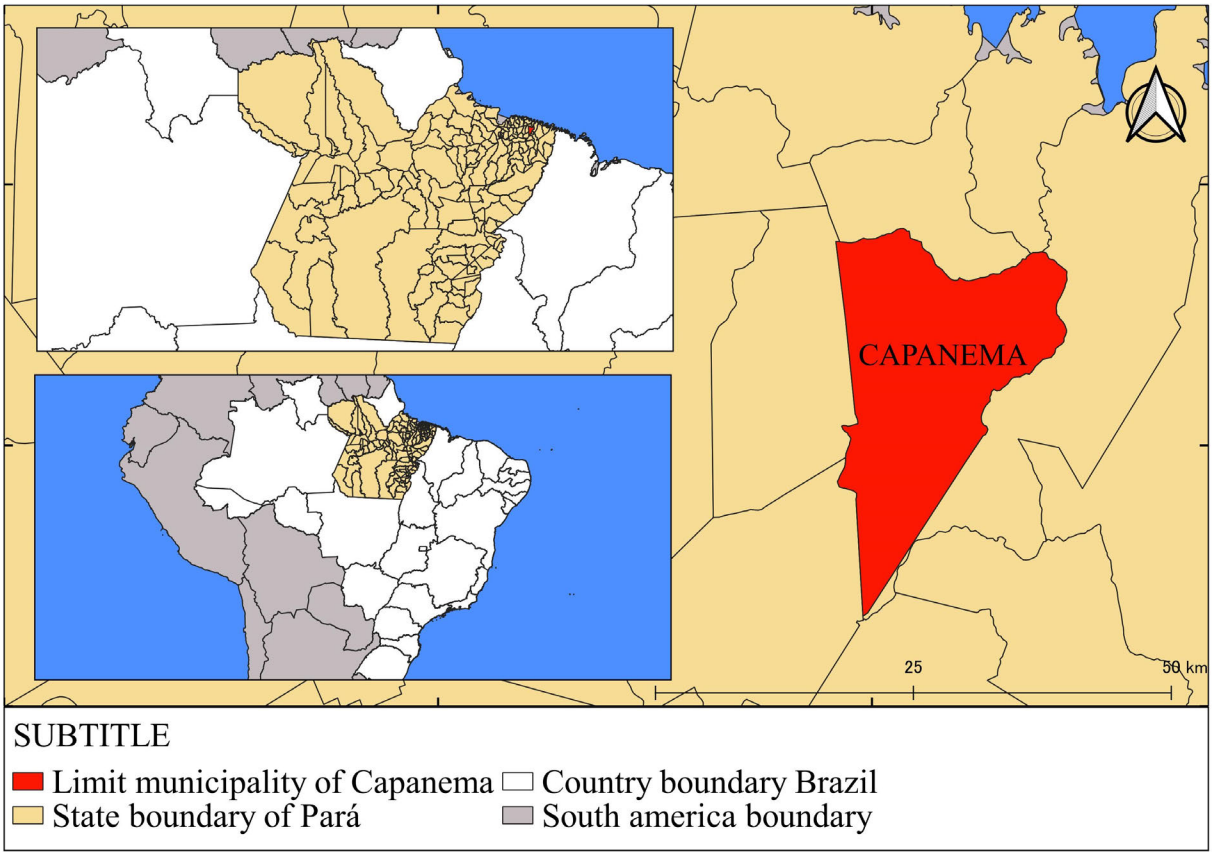

Figure 1. Location map of the study area in the Amazon rainforest, modified from (Raiol et al., 2019).

The amount of treated water lost in the state of Pará before it reaches households is staggering, equivalent to the volume of 155 Olympic-sized swimming pools or 1,890,000 liters of water. Leaks and illegal connections contribute to the loss of 292,950 liters of water per day in the state of Pará (G1 Pará, 2021). Old and dilapidated pipelines are often cited as the cause of this waste. Residents have long complained about water leaks in the streets of the study area.

From a geological point of view, the northeastern region of the state of Pará has a characteristic sedimentary package that includes rocks and sediments from the Paleogene to the Holocene, the first of which belongs to the Pirabas Formation (Cohen et al., 2005; Pereira et al., 2007). Interesting marine layers from the Pirabas Formation occur in the coastal zone, predominantly carbonate with intercalations of marl and sandstones (Antonioli et al., 2015).

From bottom to top, the study area has a sedimentary sequence consisting of 21 m thick carbonate layers of the Pirabas Formation overlain by 0.5 to 14 m thick calcareous sands and 2.0 m thick fine- to medium-grained sands with plane-parallel bedding (Rossetti et al., 2013; Aguilera et al., 2020).

3. Materials and Methods

3.1 System and data collection

3.1.1 Data acquisition

The GPR survey took place in the city of Capanema on Leandro Pinheiro Street, where water leakage occurs from a buried pipe in the middle of the street and flows onto the sidewalk following the local topography (Fig. 2a). The survey was based on area of 60 m^2 with lines spaced 0.5 m apart, forming a rectangle 10 m long (so-called Y-profiles parallel to the road) and 6.0 m wide (X-profiles perpendicular to the road) (Fig. 2b). All were recorded with a constant distance of 0.35 m between the antennas (common offset configuration) on a surface with visible leakage and an initial erosion process.

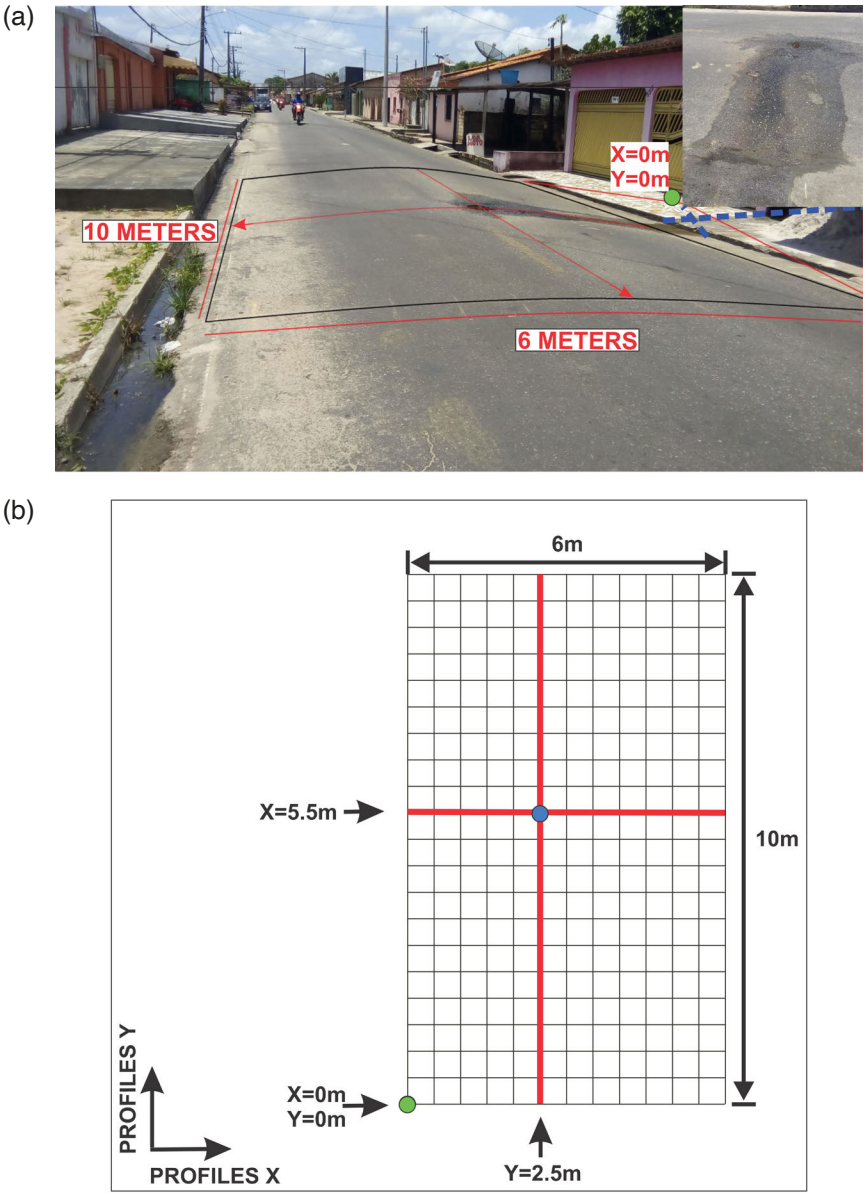

Figure 2. Area of GPR data acquisition (a). GPR profile acquisition (b). The green dot represents the X and Y origin position and the blue dot represents the position of the visible leak.

The survey was conducted with a TerraSIRch SIR (Subsurface Interface Radar) System-3000, manufactured by Geophysical Survey Systems Inc (GSSI), equipped with 400 MHz antennas, a cart, and an odometer. The antennas were selected to provide good resolution to image the pipeline and shallow subsurface to ~4 m depth. Further details of the main parameters used during data acquisition are shown in Table 2.

3.1.2 Data processing

The GPR data were processed using ReflexW software (Sandmeier et al., 1998). The processing workflow followed the steps proposed by Reis Jr. et al. (2014) and Rocha et al. (2015, 2016), which are described below: a) time zero (15.6 ns); b) background removal (between 0 and 4.2 ns); c) acquisition gain removal (no gain); d) energy decay recovery function (scaling value 1); e) dewow (2.5 ns); f) F-k filter (for kx (1/meter): 0, –3, 0, 3 and frequency in MHz: 100, 380, 800, 380, respectively); g) F-k migration; h) bandpass filter (low cutoff 80 MHz and upper cutoff 1,000 MHz), and i) time/depth conversion (e.m. wave velocity of 0.09 m/ns for f-k migration and also for time-to-depth conversion).

Parameter	Value/Details
Antennas frequency	400 MHz
Survey grid	12 line in x-direction 21 line in y-direction
Time window (Range)	150 ns
Trace spacing	0.02 m or 20 mm
Number of samples	1024 samples per trace)
Scan rate	50 scans/s
Line spacing	0.5 m
Number of lines	33
Total survey area	60 m^2 (10 m × 6 m)
Total length per line	21 line in x-direction 13 line in y-direction
Estimated number of traces per line	(10 m/0.02 m trace spacing) = 500 (6 m/0.02 m trace spacing) = 300

Table 2. Principal parameters used in this study with TerraSIRch SIR System-3000 and 400 MHz antenna.

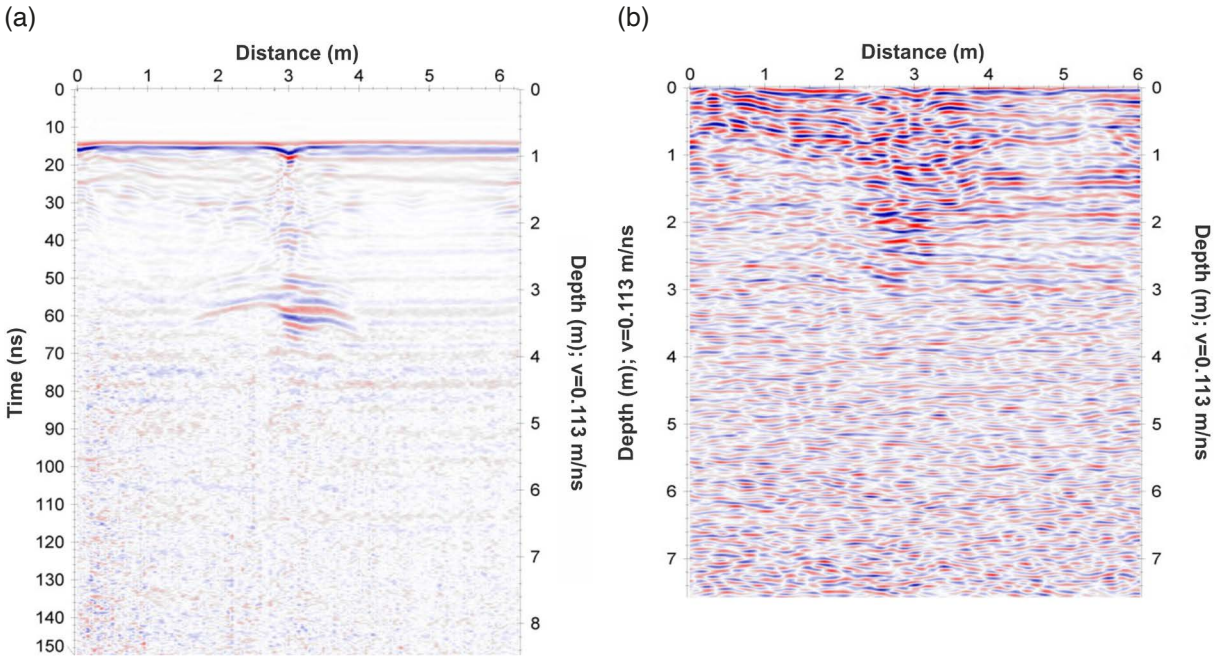

Figure 3. Radargram X12 exemplifies the data processing applied. On the left (a) the raw radargram is shown, while on the right (b) the processed radargram is shown. As highlighted, the speed of the electromagnetic wave was estimated using the hyperbolic diffraction method.

Figure 3 shows a comparison of the GPR profile before and after processing in the radargram X12 (Fig. 3). The GPR profile was corrected for time zero and the direct waves and low and high-frequency noise were removed. In addition, the corrections related to electromagnetic induction and signal attenuation with depth allowed better visualization of the depth boundary affected by the leakage (clearer amplitude reflections).

The electromagnetic wave velocity in this survey was estimated using the hyperbolic diffraction method, which examines the hyperbolic patterns formed when radar waves diffract around tiny, isolated point objects in the subsurface. Wave speed is shown by the hyperbola's apex and curvature in the GPR data. The wave velocity may be determined by measuring the difference in time between the peak and the hyperbola's edges, as well as by knowing the antenna's depth and separation. When calculating velocity in regions with isolated point-like scatterers, this approach works perfectly (Dossi et al., 2022).

The hyperbola caused by the leaky pipeline was adjusted to obtain the mean velocity used to migrate the GPR data and convert time to depth. This resulted in an average near-surface velocity of 0.09 m/ns. After this step, the processed data was interpolated, converted to SEG-Y format, and then imported into the OpendTect software to allow better visualization in a virtual 3D environment and the application of attributes (Khwanmuang and Udphuay, 2012). Thus, all GPR lines were interpolated in the ReflexW software and later inserted into the OpendTect software to better delineate the area affected by the leak.

3.1.3 Parameterization of the geophysical signal

It is well known that the GPR method identifies contrasts in electromagnetic impedance, and such variations can be associated with changes in the relative dielectric constant of the subsurface where demonstrated that the relative dielectric constant of water-saturated soils increases and consequently the impedance contrast between these areas and the rest of the soil increases, leading to reflections with higher amplitudes in the water-saturated zones (Daniels, 2000; Annan, 2003, 2009; Jol, 2008; Reis Junior et al., 2015; Lai et al., 2016; Delgado et al., 2022; Gomes et al., 2023).

The X- and Y-GPR profiles show regions with increased amplitude reflections. At a depth of up to 0.5 m, the reflections are continuous and high amplitude, characteristic of sandy layers composed mainly of quartz (Switzer et al., 2020). The reflections are slightly inclined downwards in the central part of the radargram in non-migrated profiles, with greater amplitude compared to the side (Fig. 4).

At a depth below 2.0 m, a flat blue reflection indicates a saturated zone (Fig. 4). At depths greater than this measurement, several reflections can be seen at the leak, which appears as almost evenly distributed lines and is caused by the resonance of the water at the surface (saturation) (Fig. 3). Below this point, the reflections become

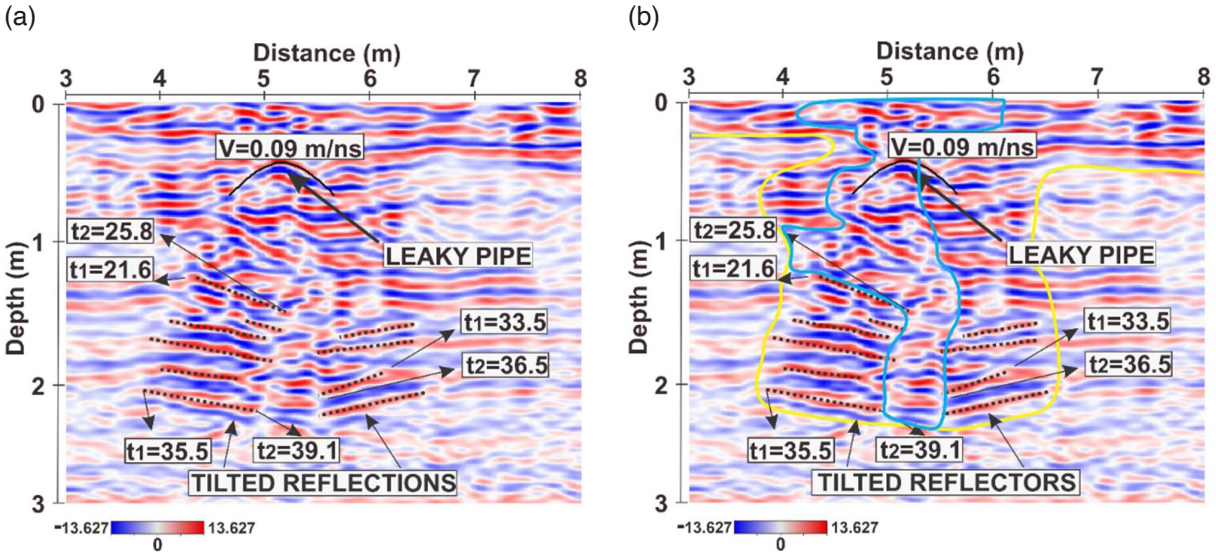

Figure 4. The left, zoomed radargram Y6 and, the right, same radargram with details showing a high amplitude (yellow line), tilted reflections within the leakage zone (dashed line), and saturated zone (blue line).

discontinuous and have a low amplitude, indicating the strong influence of the groundwater on the attenuation of the GPR signal.

We hypothesize that the layers are flat and that the inclined reflections are due to a low-velocity zone caused by water saturation in the soil near the leaky pipeline. The inclined reflections are therefore different from the parallel flat reflections characteristic of the horizontal laminated sandy interval with background moisture typical of this region, where the saturated zone is usually shallow (> 5.0 m deep).

According to Eq. 1, the EM wave propagates in the subsurface with a velocity (v) that depends on the dielectric permittivity (ε) and the speed of light in vacuum (c) (Annan, 1996). Therefore, the EM velocity decreases when passing through the water-saturated zone because the relative dielectric constant increases with water saturation.

$$v = \frac{c}{\sqrt{\varepsilon}} \tag{1}$$

Table 3 shows the increased relative dielectric constant of water compared to air and its high ability to influence other materials. An abrupt increase in the relative dielectric constant can also be observed when comparing a dry

Material	ε_r	σ (S/m)	v (m/ns)	α (dB/m)
Air	1	0	0.3	0
Freshwater	80	0.01-0.05	0.033	0.1-1
Seawater	70	3-5	0.036	1000-3000
Dry Sand	3-5	$\sim 10^{-6}$	0.13-0.17	0.01-0.1
Wet Sand	15-30	$\sim 10^{-3}$	0.055-0.077	1-10
Dry Soil	2-6	$\sim 10^{-5}$-10^{-4}	0.12-0.21	0.1-1
Moist Soil	10-15	$\sim 10^{-3}$	0.077-0.095	1-10
Clay	5-40	1-10	0.047-0.13	10-100
Ice	3-4	$\sim 10^{-6}$	0.15-0.17	0.01-0.1
Granite	4-6	$\sim 10^{-6}$	0.12-0.15	0.1-1
Limestone	4-8	$\sim 10^{-6}$	0.11-0.15	0.1-1
Concrete	4-10	$\sim 10^{-2}$	0.095-0.15	1-10
Asphalt	3-5	$\sim 10^{-5}$	0.13-0.17	0.1-1
Wood	2-6	$\sim 10^{-4}$	0.12-0.21	0.1-1

Table 3. Typical Values of relative dielectric constant (ε_r), electrical conductivity (σ), velocity (v), and attenuation (α) of some materials, modified from (Davis and Annan, 1989; Zeng and McMechan, 1997; Jol, 2008).

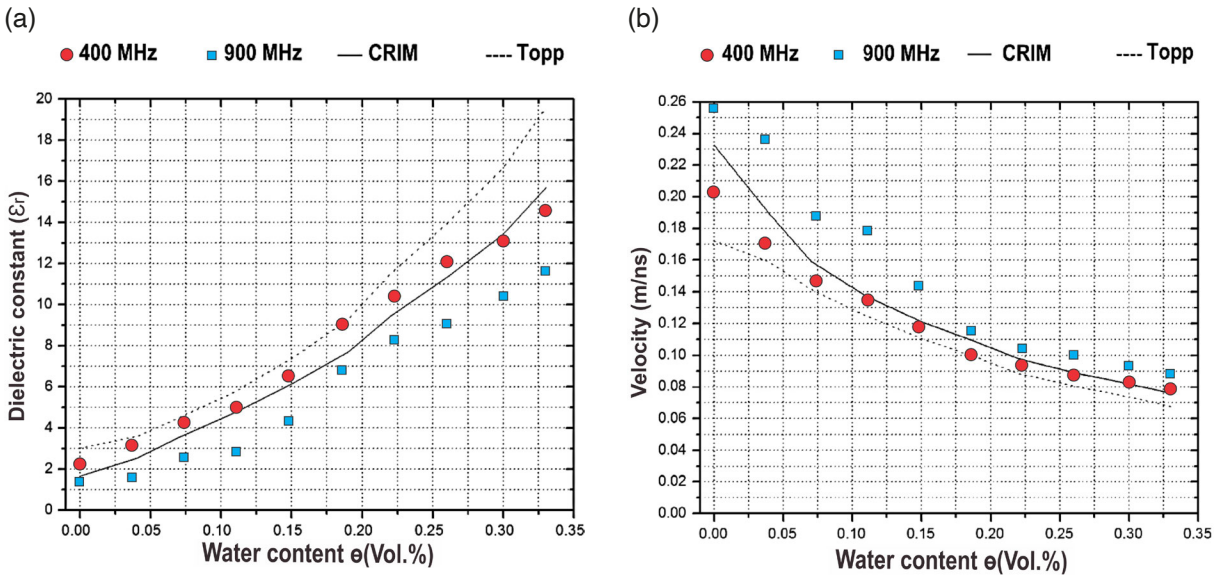

Figure 5. Cross plots of the water content against the relative dielectric constant (A) and the water content against the propagation velocity of the electromagnetic wave (B). The red circles indicate measurements made with 400 MHz antennas on the sand and the blue squares with 900 MHz antennas. The solid and dotted lines represent empirical curves associated with the Wyllie and Gregory method and the Topp equation, modified after (Topp et al., 2002; Wyllie and Gregory, 1953).

and moist geological material. This explains the particular behavior of electromagnetic waves in the water-saturated zone in sedimentary layers and makes it possible to visualize and delineate this anomalous region in the GPR images.

This GPR response is consistent with the experiments of Van Dam et al. (2013), Bradford (2007), Lambot et al. (2004), and Schmalz and Lennartz (2002). These studies investigated the effectiveness of the Complex Refractive Index Model (CRIM) proposed by Birchak et al. (1974) and the Topp equation, proposed by Topp et al. (1980) for soil moisture estimation, emphasizing their respective strengths and limitations across different contexts (Figs. 5a and 5b, respectively). While the Topp equation is straightforward and widely used, the CRIM model, when applied with proper calibration and parameterization, offers a more flexible approach to estimate dielectric properties, especially in complex or heterogeneous media.

These studies explored the efficacy of the CRIM model and the Topp equation in soil moisture estimation and highlighted their strengths and limitations in various contexts. While the Topp equation is straightforward and widely used, the CRIM model, when applied with proper calibration and parameterization, offers a more flexible approach to estimate dielectric properties, especially in complex or heterogeneous media.

3.2 System and data collection

3.2.1 Synthetic radargram

A synthetic radargram was created to better understand the anomalous GPR signal caused by leakage and to test the best input attributes and parameters for this investigation. The GPR model was created using ReflexW software, which uses an algorithm based on the finite-difference time-domain (FDTD) (Sandmeier, 1998). The software creates a discrete system model for GPR profiling consisting of a 2D geometric mesh (Babuska et al., 2012). In addition, the geophysical model was extended beyond its original length to avoid unwanted boundary effects. Therefore, the geometric model used to generate the 10 m long synthetic GPR images has a total extension of 50 m.

The simulations were performed with a center frequency of 400 MHz, a spatial increment of 0.04 m, and a temporal increment of 0.06 ns, calculated by the software itself, respecting the numerical stability criterion and giving the system convergence conditions (Sandmeier, 1998; Babuska et al., 2012; Taflove and Brodwin, 1975).

For the simulation of electromagnetic wave propagation in the subsurface, the flat wave option was used. The geometric model developed consists of plane-parallel layers (Fig. 6a) and the synthetic radargram generated for this

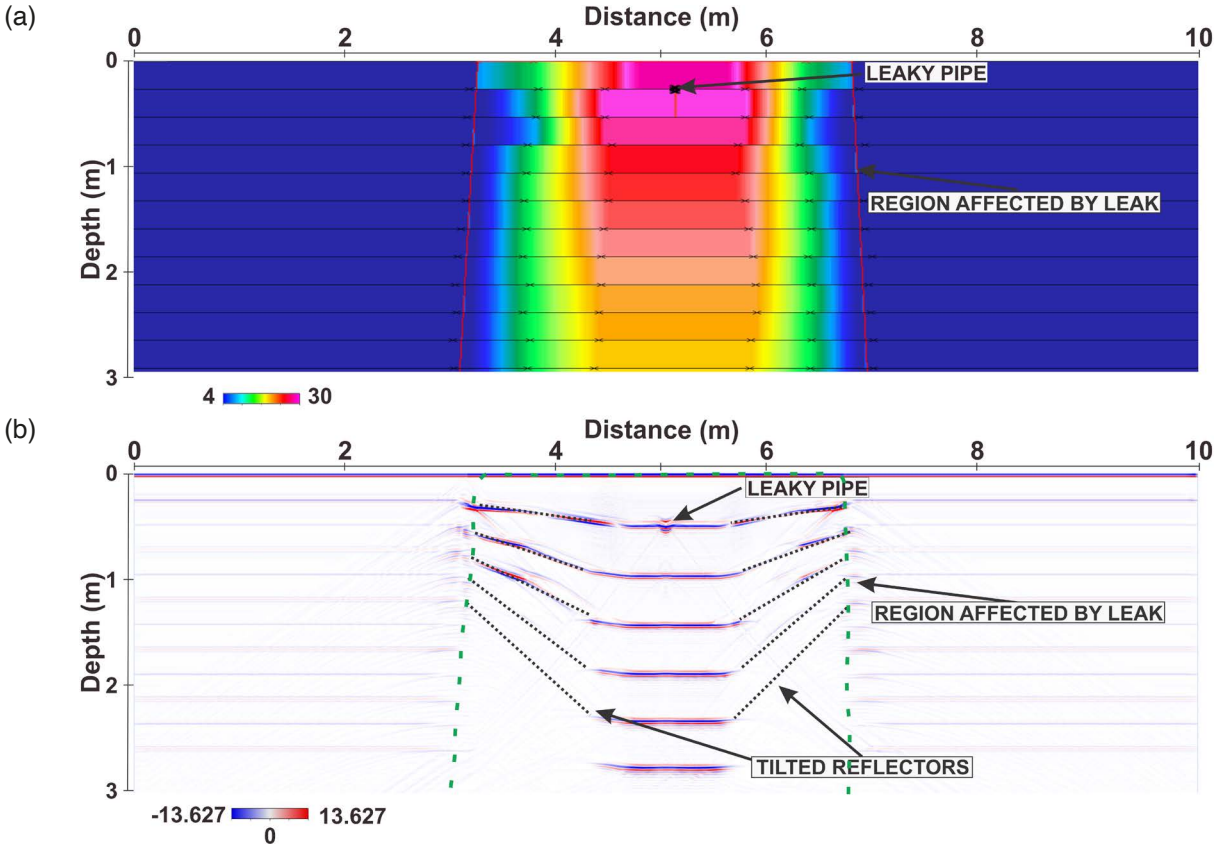

Figure 6. Geophysical model of the underground water leakage (a). The red lines represent the region of soil partially saturated with water (light blue to dark green). Synthetic radargram generated from the geophysical model (b). The green lines represent the region affected by the water leakage.

model (Fig. 6b). The relative dielectric constant of each layer varied between 4 and 4.5 to produce sufficient contrast in the electromagnetic impedance between the layers and corresponded to the properties and characteristics of the subsurface, as shown in Table 4.

Sedimentary Features	ε_r	σ (S/m)
Infiltrated zone	10-30	0.0001
Sandy deposit	5	0.00001
Calciferous sand	4-4.5	0.00001

Table 4. Physical parameters used for the synthetic radargram. Relative dielectric constant (ε_r) and electrical conductivity (σ) in S/m.

A cylindrical volume with a relative dielectric constant f 80 simulates a pipe filled with water. Above the central part of the model, the top layer represents the water-saturated area created by the water leak in the subsurface. The relative dielectric constant varies between 10, the outermost part, and 30, the innermost part. The electrical conductivity did not vary, for the sake of simplifying the model. The zone with the highest relative dielectric constant value corresponds to the highest concentration of infiltrated water near the pipe. In this model, the saturated region was inserted throughout the region, not only above the leak.

Figure 6b shows the synthetic radargram. The green dotted line delimits the area affected by the water leak, which has a higher reflection amplitude than the outer part. It is noteworthy that the reflections are inclined downwards due to the decrease in electromagnetic wave velocity. The low velocity of the electromagnetic waves in the leakage zone causes a propagation delay that pushes the reflections below the zone of velocity anomaly downwards.

Nobes et al. (2010) described velocity dips in GPR profiles due to a loess wedge at the base of the Ostler Fault (New Zealand), which were initially interpreted as folds or infilled channels. A systematic velocity analysis shows that the electromagnetic wave velocity of loess is 15 -20% lower than that of the surrounding sandy gravels, resulting in time delays of 10 to 15 ns.

3.2.2 The reflector tilt method (RTM)

In addition to the hyperbola adjustment technique, in which the velocity is determined by a curve fitting procedure superimposed on a typical hyperbolic curve, a novel approach enables the calculation of the mean relative dielectric constant and the velocity: the reflector tilt method (RTM). It assumes that the presence of water in the pores of unconsolidated, horizontally stratified sand layers changes their relative dielectric constant and velocity, which leads to a delay in the arrival time of the reflections.

As a result, the GPR profiles show horizontal reflections in dry zones (not-saturated zone), which are unaffected by water leakage, and increasingly inclined reflections towards the center of the saturated zone (water-filled pores - low velocity). In other words, the electromagnetic waves traversed the sand layers with laterally different dielectric constants and velocities that triggered the observed inclination of the reflections, which were originally intended to be horizontal. This effect is similar to that found in reflection seismic in high-velocity zones within pre-salt layers (Blondel et al., 2022; Uranga et al., 2024). However, in this example, the inclination is reversed, as there is an increase in velocity, whereas in this research, there is a decrease in velocity, resulting in a downward inclination.

Therefore, water saturation is the decisive factor: the higher it is, the lower the wave velocity and the stronger the inclination of the reflection. The water-saturated zone is located near the leak and above the pipe, in the center of the infiltrated area. The angle of inclination is proportional to the difference between the propagation velocity in the not-saturated zone and the water-saturated zone.

A simplified model is used to illustrate this fact in Fig. 7, where a horizontal reflector is inclined at an angle (θ). The opposite side of this angle equals the two-way travel time of wave propagation in the water-saturated zone (t_2), minus the two-way travel time of wave propagation in the unsaturated zone (t_1). Thus, the inclination angle θ is given by Eq. 2:

$$\theta = \tan^{-1}\left(\frac{t_2 - t_1}{\Delta x}\right) \tag{2}$$

where Δx is the distance between the farthest point of the inclined reflection and the point where the inclination begins. Thus, knowing that:

$$t_1 = \frac{h}{v_1} \tag{3}$$

$$t_2 = \frac{h}{v_2} \tag{4}$$

where v_1 is the mean velocity used to convert time to depth (the hyperbolic velocity in the unsaturated zone), and v_2 is the velocity in the water-saturated zone, it becomes evident that:

$$\theta = \tan^{-1}\left[\frac{h\left(\frac{1}{v_2} - \frac{1}{v_1}\right)}{\Delta x}\right] \tag{5}$$

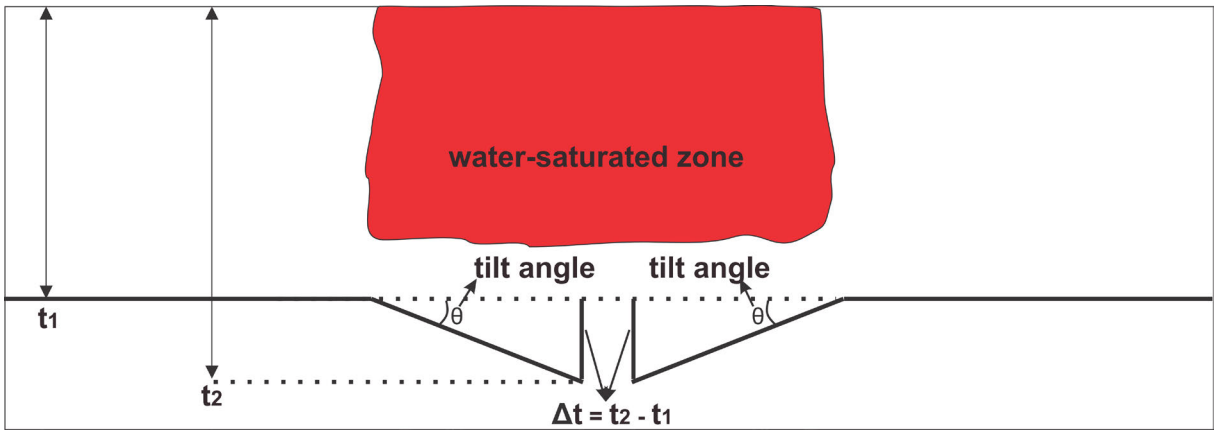

Figure 7. Simplified model showing the slope of reflections below the water-saturated zone.

and substituting the velocity (v) given in Eq. 1, we have that:

$$\theta = \tan^{-1}\left[\frac{\frac{h}{c}(\sqrt{\varepsilon_2} - \sqrt{\varepsilon_1})}{\Delta x}\right] \tag{6}$$

Considering the time delay of horizontal reflections between unsaturated and saturated zones, we can not only map the leakage zone but also calculate the interval velocities in Eq. 7 and Eq. 8. It is known that:

$$v_1 t_1 = v_2 t_2 \tag{7}$$

The velocity equation used for the water-saturated zone is:

$$v_2 = \frac{v_1 t_1}{t_2} \tag{8}$$

By replacing the times (t_1) and (t_2), presented in Fig. 6, and the mean velocity used to convert time to depth, it yields the mean value of 0.08 m/ns for the water-saturated zone. Once v_2 is calculated, Eq. 1 determines the relative dielectric constant for the water-saturated zone site which was approximately 14.2 (Table 5).

3.2.3 GPR attributes

Seismic attributes enhance the interpretation of 3D seismic data by highlighting features like faults (coherence), folds (curvature), and lithology changes (spectral components). While effective in identifying subtle details, they can also magnify issues such as acquisition footprints and velocity anomalies (pull-up/push-down). Accurate imaging with prestack depth migration (PSDM) and a proper velocity model can mitigate false structures, but without thorough PSDM and velocity analysis, conventional amplitude and attribute interpretation may lead to significant errors (Marfurt and Alves, 2015).

Traditional interpretations of GPR data in areas of subsurface leakage are generally based on variations in trace amplitude, which can limit interpretations (Lai et al., 2016; Diamanti and Annan, 2019). However, the GPR attributes are based on mathematical calculations of the amplitude data, which highlight areas of high amplitude as the zone affected by the water leak, which is the case in this study.

Reflections	t_1 (ns)	t_2 (ns)	Velocity water-saturated zone (m/ns)	Average velocity water-saturated zone (m/ns)	Average velocity not-saturated zone (m/ns)	Relative dielectric constant	Average of relative dielectric constant
1	35.5	39.1	0.082	0.08	0.090	13.479	14.174
2	21.6	25.8	0.075			15.852	
3	33.5	36.5	0.083			13.190	

Table 5. Values used in the simulations of the synthetic radargram to calculate the relative dielectric constant in the saturated zone.

Various GPR attributes are essential for analyzing and interpreting GPR data. The attributes are categorized into several types, for example: a) instantaneous attributes that are derived from complex trace analysis and include reflection strength (instantaneous amplitude) and instantaneous phase, calculated using the Hilbert transform. The instantaneous frequency, which is the first derivative of the instantaneous phase, is also included; b) amplitude-related attributes that focus on variations in amplitude along GPR traces. Common calculations include Root Mean Square (RMS) and energy, which is defined as the ratio of the sum of squared sample values within a specified time window to the number of samples; c) frequency-related attributes that are derived from the frequency content of the GPR signals and help in understanding the spectral characteristics of the data; d) coherency attributes that attributes measure the continuity and coherence of reflections, which can indicate the presence of geological features; and e) texture attributes that assess the texture of the data, providing insights into the spatial distribution and arrangement of geological features.

These attributes can significantly enhance the interpretation of GPR datasets by providing quantifiable parameters that represent subsets of the information contained in the original data. Table 6 summarizes the principal types of attributes used in previous studies and highlights their sensitivity to various geological and structural features (Chen and Sidney, 1997; Chopra and Marfurt, 2007; McClymont et al., 2008; Forte et al., 2012; Allroggen and Tronicke, 2016; Ercoli et al., 2021).

Therefore, some attributes were tested with mathematical calculations applied to the amplitudes of the collected data, such as average, median, min, max, sum, variance, norm variance, most frequent, and root mean square (RMS) (Forte et al., 2012; Reis Jr et al., 2014; Klewe et al., 2021; Joshaghani and Shokrabadi, 2022).

However, the energy, amplitude variance, and RMS amplitude attributes show promising results. The energy attribute calculates the ratio between the sum of the squares of the amplitudes and the number of samples within a given time window in Eq. 9 (Forte et al., 2012). The window length must have approximately the wavelength value of the signal's center frequency. This attribute highlights reflections with low and irregular amplitudes and individualizes sequences with different electromagnetic impedance contrasts:

$$E(n) = \frac{\sum_i^n {a_i}^2}{n} \tag{9}$$

where n is the number of samples, and a is the amplitude of these samples in a given section of the GPR trace.

The amplitude variance determines the deviation of the signal energy from the mean of the expected value in a given sample window in Eq. 10. The presence of water in the soil modifies the electromagnetic impedance so that the received signal increases statistical characteristics, such as variance (DX), which determines the deviation of the signal energy from the expected average value:

$$Var(X) = \frac{\sum_{i=k_1}^{k_n} (X_i - \overline{X})^2}{n} \tag{10}$$

Attribute	Sensitivity
Instantaneous Attributes	Sensitive to short-term changes in amplitude, phase, and frequency. Useful for detecting fine-scale variations in the seismic signal.
Amplitude-Related Attributes	Sensitive to changes in reflection strength and impedance contrasts. Indicates lithological variations and fluid content.
Frequency-Related Attributes	Sensitive to the thickness of layers, bed tuning, and stratigraphic details. Helps identify thin beds and hydrocarbon indicators.
Coherency Attributes	Sensitive to lateral continuity and structural discontinuities such as faults and fractures. Useful for identifying faults, fractures, and stratigraphic boundaries.
Texture Attributes	Sensitive to spatial variation patterns in amplitude, capturing geological textures, stratigraphic variations, and depositional environments.
Sample-to-Sample Differences	Sensitive to abrupt changes between adjacent seismic samples. Highlights small-scale features like fractures and faulting.
Contrast Similarity (CS)	Sensitive to reflection strength and contrast between adjacent seismic traces, highlighting stratigraphic and structural boundaries.
Structural Similarity (SS)	Sensitive to spatial consistency in amplitude patterns across adjacent traces, useful for assessing structural and stratigraphic continuity.

Table 6. Characteristics of principal attributes highlight their sensitivity to various geological or structural features, modified from (Allroggen and Tronicke, 2016).

where X_i corresponds to the signal amplitude; X is the average signal amplitude value, and the interval from K_1 to K_n in the sum corresponds to the time window considered in the data analysis; and n corresponds to the number of samples in the trained time interval. In contrast, the root mean square (RMS) calculates the average of the sum of the squares of the amplitudes in a given analysis window and is very sensitive to extreme values (Klewe et al., 2021; Liu et al., 2020). After several tests, we chose an optimal time window of 40 ns for all attributes.

Figure 8 shows the modeled GPR image with the original amplitude (Fig. 8a) and the attributes energy, variance, and RMS amplitude. The attributes delimit the infiltration zone. The energy (Fig. 8b) and RMS attribute (Fig. 8d)

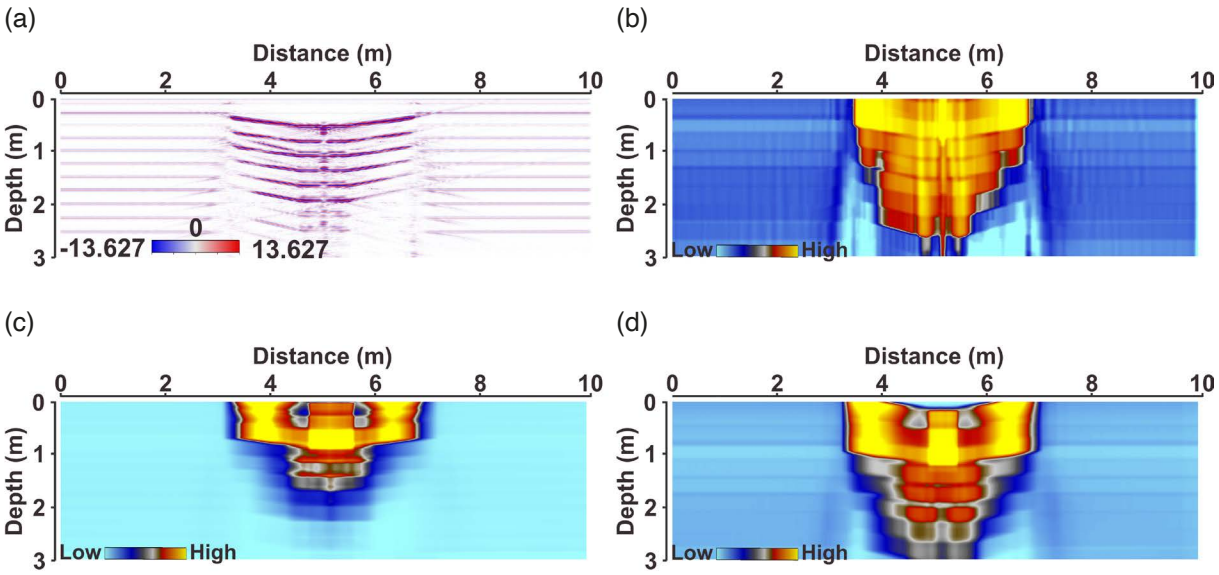

Figure 8. Synthetic radargram (A) and the attributes used to identify the infiltration zone: Energy (B), Variance Amplitude (C), and RMS Amplitude (D).

provided a better response in delineating the two zones affected by the leakage (Zones A and B). The amplitude variance attribute (Fig. 8c) shows a tendency towards a vertical reduction of the leakage geometry, which is probably due to the low contrast of the electromagnetic impedance and the attenuation of the electromagnetic waves at depth.

4. Results and Discussions

In this study, various data processing techniques were employed to analyze the GPR data. Notably, the RTM was applied exclusively to the real GPR datasets collected from the urban pavements. The GPR profiles X12 and Y6 cross the leakage zone in the subsurface (Fig. 2). After calibrating the mathematical input parameters of the GPR attributes in the synthetic profile, the attributes were then tested in the actual GPR data. Figure 9 shows the GPR profile Y6 and its attributes of energy, amplitude variance, and RMS amplitude.

The results are very similar to those of the synthetic data (Fig. 6). Indirectly, the similarity between the synthetic and the real data shows that the proposed model is very realistic concerning the physical properties of the study area, despite the simplicity of the model geometry of the layers and the subsurface water leakage zone.

GPR data can indicate the maturity of the leakage based on geophysical criteria to infer how long the leak has existed. The maturity of the leak follows a trend from an early to an advanced stage based on the change over time in the volume increase of the affected area or the presence of voids and cavities created by water-bearing sediments.

The following signs indicate that this is a typical case of early-stage leakage: a) the mean value of the dielectric constant, which lies between dry and water-saturated sand; b) advanced stages of water saturation make it difficult to identify the hyperbola, which is only visible in early-stage leakage; c) the slope of the reflections indicates that most of the area covered by the GPR survey was partially saturated with water due to the leakage, and clearly shows the boundary between the infiltrated and unaffected zone (Fig. 9); d) the absence of erosion features such as voids and the collapse of the dome associated with the affected area. These features are typical of an advanced stage of leakage.

The chaotic and interrupted reflection pattern in the central areas of Figs. 3, 4, 6, 8, and 9 and the columnar geometry with bifurcations in the middle and top of Fig. 4 indicate the affected area. The GPR profile of this zone shows the preferred water paths: from the leak upwards to the surface and downwards to a depth of 2.4 meters.

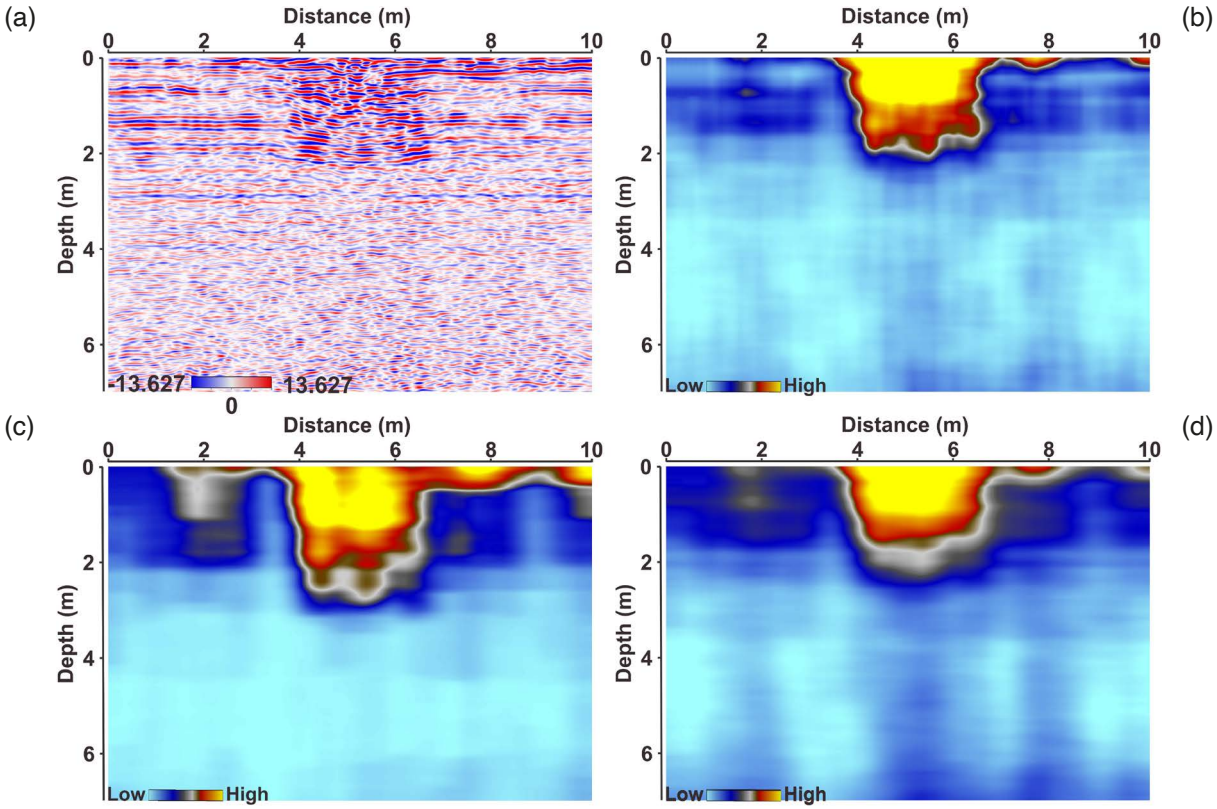

Figure 9. Radargram of the GPR profile Y6. In the sequence, we processed the profile with the steps described in Table 2 (A) and after applying the attributes: Energy (B), Amplitude of Variance (C), and Amplitude RMS (D).

The irregularities in the groundwater distribution are probably related to heterogeneous surfaces, which in this case study, the anomalous reflection pattern and the attributes of the GPR provide an accurate picture of water leakage and preferred water flow (see blue line in Fig. 4).

This is because the hydraulic parameters are distributed differently depending on the heterogeneity of a sand body and the method used to measure it, such as GPR or hydraulic soil modeling. While most attributes do not allow a quantitative study of hydrologic properties, they can be very helpful in defining their variance, which can be very useful for example to describe how susceptible soil-water systems are to preferential flow.

The attributes delineate the leakage zone very well. Among all attributes, the energy attribute provides a better result, as the area with higher energy was better highlighted (red and yellow zones in Fig. 8b). In addition, the external geometry is more similar to the high amplitude zones in the original radargram (Fig. 8a). Although the variance (Fig. 10c) and RMS (Fig. 8d) attributes also emphasize the leakage zone, they show intermediate values (light brown color) in other zones outside the affected area.

Fig. 10a shows a three-dimensional perspective of profiles X12 and Y6, and Fig. 10b shows the energy time slice at 1.0 m depth. Figure 10c shows an intersection of the GPR profiles with the energy time slice at 1 m depth. We recognize the high-energy zone caused by the increase of EM impedance contrast in the leakage zone (the yellow-colored area).

An energy cube in the investigation area enables a depth characterization of the leakage zone. In addition, the isosurface technique was applied to the energy attribute to map the 3D geometry of the water leakage (Fig. 11). The area affected by the leak has an irregular geometry but was perfectly delineated. It measures approximately 4.0 m in length and 3.15 m in width at the top and decreases in size with increasing depth. We observed that the plume decreases with depth, possibly due to two facts: either the plume has reached the static level or the concentration in the vadose zone has decreased.

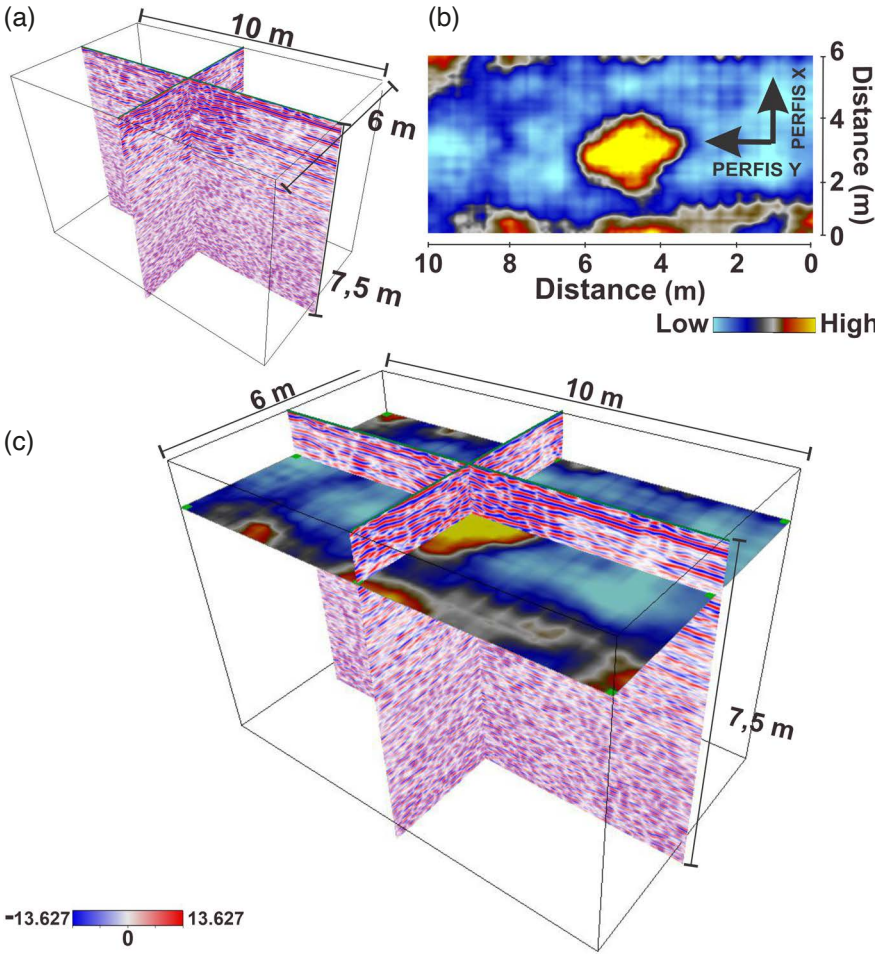

Figure 10. Radargram of the GPR profile Y6. In the sequence, we processed the profile with the steps described in Table 2 (A) and after applying the attributes: Energy (B), Amplitude of Variance (C), and Amplitude RMS (D).

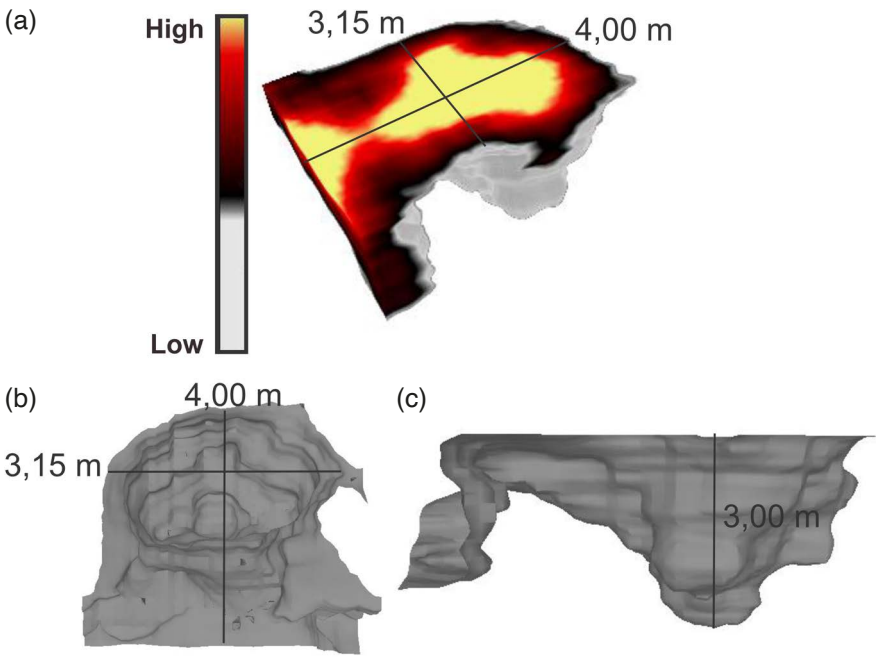

Figure 11. Schematic 3D model of the Energy cube, showing the estimated volume of the water leakage area (A), top view of the Energy Isosorbide (B), and side view of the Energy Isosurface (C).

The volume of the leakage zone mapped with the GPR is about 20 m^3. The infiltration depth reached 3.0 m (Figs. 11b and 11c), indicating that a large volume of leaking water, as seen in Fig. 2a, would probably leak due to the high water pressure and shallow pipe depth of about 0.5 m, as shown in the hyperbola in the center of Fig. 4.

Figure 12 shows a 3D view of the isosurface energy technique with radargrams X1, Y6, and Y12, showing the good correlation between the isosurface energy and the high amplitude regions caused by the increase in relative dielectric constant in the region where the Y6 profile was recorded. It can also be seen that in the regions not affected by the leak (X1 and Y12), the reflections are plane-parallel due to the sand layers in the study area. The ellipse identifying the pipe is highlighted in yellow.

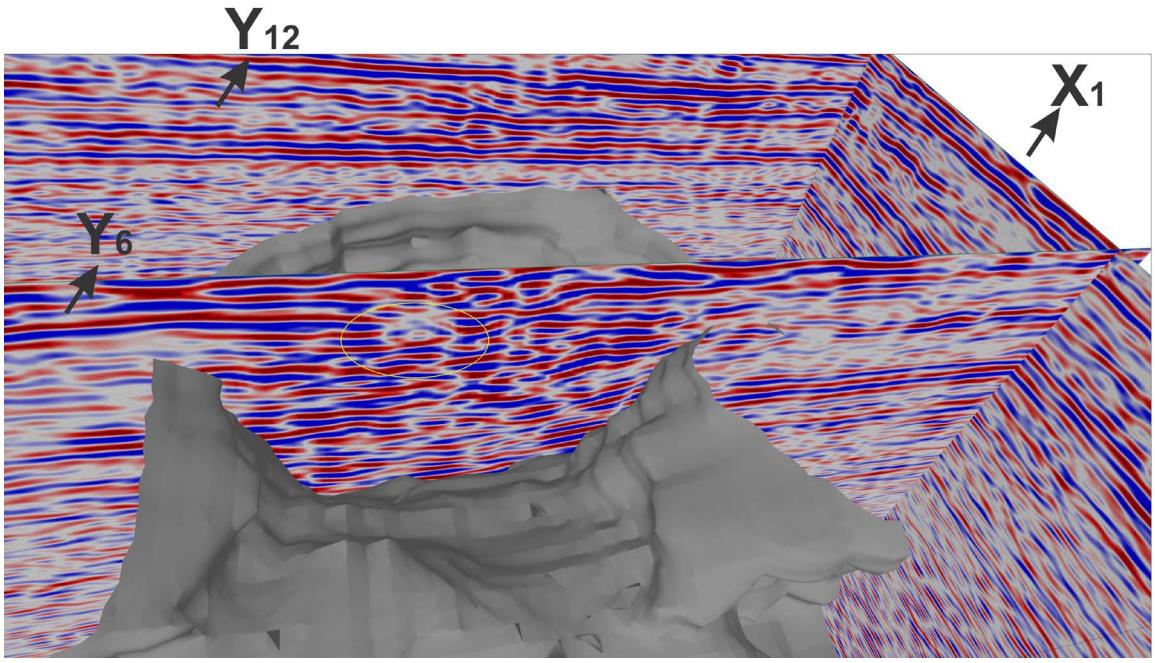

Figure 12. 3D view of the isosurface energy technique with the X1, Y6, and Y12 radargrams.

Despite the successful delineation of the wetland in this work, we suggest other possibilities, such as using the isosurface technique with other attributes to delineate anomalous zones under less favorable conditions than those observed in this study.

5. Conclusions

The use of GPR surveys at a frequency of 400 MHz has proven to be very effective in detecting water leaks in urban pavements in the Amazon region. Analysis of the GPR data revealed clear patterns of water saturation that allowed accurate identification of affected and unaffected areas.

The application of advanced processing techniques, including attribute analysis and three-dimensional modeling, significantly improved the interpretation of the GPR data. Key attributes such as energy and energy isosurface played a crucial role in accurately determining the geometry and volume of the infiltration zones and provided important insights into the extent of water infiltration.

This study sheds light on the characteristics of infiltration zones created by water leaks by revealing their three-dimensional conical geometry and elliptical horizontal cross-section. In addition, the study observed the infiltration of water both downward and upward from the leak site, with depths of up to 3 meters and an estimated volume of the water leakage area.

Recommendations are made for the use of reverse time migration and attribute analysis, particularly in scenarios where water is leaking in resistant, porous, horizontally layered sand layers. These methods prove to be effective in estimating the relative dielectric constant of infiltration zones and detecting reflection gradients caused by delays in electromagnetic wave propagation.

The method developed in this study is suitable not only for the detection of water leaks, but also for tasks such as measuring pavement thickness, inspecting bridges and tunnels, and detecting hydrocarbon leaks at gas stations. Integration with multi-temporal surveys provides information on the geometric evolution of contamination plumes and helps to formulate environmental recovery strategies. It should be noted that high moisture content, clayey soils, conductive materials such as metal and salt water, and thick asphalt layers can limit the effectiveness of the method as they significantly attenuate the GPR signals.

Further research and development are essential to refine and extend the applicability of the proposed methodology. Future studies should focus on optimizing processing techniques for infrastructure projects and exploring the potential of multi-temporal surveys for long-term monitoring. Such efforts will provide accurate and reliable data for geophysicists, geotechnical, and civil engineers and contribute to effective environmental assessment and management of urban infrastructure and risk mitigation in the Amazon region of Brazil and potentially beyond.

Data availability statement. The datasets generated and analyzed during the current study are available from the corresponding author upon reasonable request. These datasets include Ground Penetrating Radar (GPR) data collected in situ, as well as the synthetic data produced through computer modeling. Access to the data may be subject to ethical considerations and institutional policies.

Acknowledgements. The authors would like to thank the Faculty of Geophysics (FAGEOF) at the Federal University of Pará (UFPA) for providing the TerraSIRch SIR System-3000 equipment during the data acquisition phase. In addition, the authors acknowledge the support of the Scientific and Technological Initiation Program (PIBIC) at the Federal Rural University of Amazônia (UFRA), which provided a scholarship to the third author. Special thanks to the Laboratory of Stratigraphic Analysis (LAE) at the Federal University of Rio Grande do Norte (UFRN) for granting access to the software licenses (ReflexW and OpendTect) used during the modeling and processing phases of the GPR data. The authors extend sincerely thank the reviewers for their valuable contributions, which have significantly enhanced the discussions and overall quality of this article. Your insightful feedback has helped us refine our analysis and improve the clarity of our findings.

References

Adedeji, K., Y. Hamam, B. T. Abe and A. Abu-Mahfouz (2017). Leakage Detection and Estimation Algorithm for Loss Reduction in Water Piping Networks, Water, 9, 10, 773, doi:10.3390/w9100773.

Aguilera, O., K. Bencomo, O. M. O. de Araújo, B. B. Dias et al. (2020). Miocene heterozoan carbonate systems from the western Atlantic equatorial margin in South America: The Pirabas Formation, Sediment. Geol., 407, 105739, doi:10.1016/j.sedgeo.2020.105739.

Allroggen, N. and J. Tronicke (2016). Attribute-based analysis of time-lapse ground-penetrating radar data, Geophysics, 81, 1, H1-H8, doi:10.1190/geo2015-0171.1.

Annan, A. P. (1996). Transmission dispersion and GPR, J. Environ. Eng. Geophys., 1, 125-136, doi:10.4133/JEEG1.B.125.

Annan, A. P (2009). Electromagnetic principles of ground penetrating radar, Ground Penetrat. Radar Theory Appl., 1, 3-40, doi:10.1016/B978-0-444-53348-7.00001-6.

Annan, P. (2003). Ground Penetrating Radar Principles, Procedures and applications, Sensors and Software Inc., 286.

Antonioli, L., V. de Araújo Távora and R. Dino (2015). Palynology of carcinolites and limestones from the Baunilha Grande Ecofacies of the Pirabas Formation (Miocene of Pará state, northeastern Brazil), J. S. Am. Earth Sci., 62, 134-147, doi:10.1016/j.jsames.2015.05.005.

Ayala-Cabrera, D., E. Campbell, E. P. Carreño-Alvarado, J. Izquierdo et al. (2014). Water leakage evolution based on GPR interpretations, Procedia Eng., 89, 304-310, doi:10.1016/j.proeng.2014.11.192.

Azarhoosh, A. and S. Pouresmaeil (2020). Prediction of Marshall Mix Design Parameters in Flexible Pavements Using Genetic Programming, Arab. J. Sci. Eng., 45,10, 8427-8441, doi:10.1007/s13369-020-04776-0.

Babuska, I., J. E. Flaherty, W. D. Henshaw, J. E. Hopcroft et al. (2012). Modeling, Mesh Generation, and Adaptive Numerical Methods for Partial Differential Equations, Springer, 75, doi:10.1007/978-1-4612-4248-2.

Birchak, J. R., C. G. Gardner, J. E. Hipp and J. M. Victor (1974). High dielectric constant microwave probes for sensing soil moisture, Proc. IEEE, 62, 93-98, doi:10.1109/PROC.1974.9388.

Blondel, S., J. Ford, A. Lockwood, A. Del Ben et al. (2022). Reprocessed 2-D airgun seismic reflection data SALTFLU (salt deformation and sub-salt fluid circulation in the Algero-Balearic abyssal plain) in the Balearic promontory and the Algerian basin, Earth Syst. Sci. Data Discuss., 2022, 1-30, doi:10.1007/s11001-023-09512-5.

Bradford, J. H. (2007). Frequency-dependent attenuation analysis of ground-penetrating radar data, Geophysics, 72, 3, J7-J16, doi:10.1190/1.2710183.

Canestrari, F. and L. P. Ingrassia (2020). A review of top-down cracking in asphalt pavements: Causes, models, experimental tools and future challenges, J. Traffic. Transp. Eng. (Engl. Ed.), 7, 5, 541-572, doi:10.1016/j.jtte.2020.08.002.

Chen, Q. and S. Sidney (1997). Seismic Attribute Technology for Reservoir Forecasting and Monitoring, Lead. Edge, 16, 445-456, doi:10.1190/1.1437657.

Chopra, S. and K. J. Marfurt (2007). Seismic attributes for prospect identification and reservoir characterization, Ed. SEG/EAGE, 481, doi:10.1190/1.9781560801900.

Cohen, M. C. L., P. W. M. Souza Filho, R. J. Lara, H. Behling et al. (2005) A model of Holocene mangrove development and relative sea-level changes on the Bragança Peninsula (Northern Brazil), Wetl. Ecol. Manag., 13, 4, 433-443, doi:10.1007/s11273-004-0413-2.

Daniels, J. J. (2000). Ground penetrating radar fundamentals, Prepared as an appendix to a Report to the U.S. EPA, Region V, Nov. 25, Ohio State University, Columbus, 1-21.

Davis, J. L. and A. P. Annan (1989). Ground,Äêpenetrating radar for high,Äêresolution mapping of soil and rock stratigraphy, Geophys. Prospect., 37, 5, 531-551, doi:10.1111/j.1365-2478.1989.tb02221.x.

De Coster, A., J. P. Medina, M. Nottebaere, K. Alkhalifeh et al. (2019). Towards an improvement of GPR-based detection of pipes and leaks in water distribution networks, J. Appl. Geophys., 162, 138-151, doi:10.1016/j.jappgeo.2019.02.001.

De Souza Moreira, J., M. C. L. Paula, W. R. Borges, A. L. F. Santos et al. (2022). Ground Penetrating Radar applied to asphaltic pavements – a study in a controlled site, Braz. J. Geophys., 40, 1, 53-63, doi:10.22564/brjg.v40i1.2133.

Delgado, L. F. S., P. A. C. Oliva, M. El Robrini and J. A. dos Reis Júnior (2022). Contribution of Ground Penetrating Radar in the study of an Amazon tide channel, influenced by macro tide, J. S. Am. Earth Sci., 116, 103776, doi:10.1016/j.jsames.2022.103776.

Diamanti, N. and A. P. Annan (2019). Understanding the use of ground-penetrating radar for assessing clandestine tunnel detection, The Leading Edge, 38, 6, 453-459, doi:10.1190/tle38060453.1.

Dossi, M., E. Forte, B. Cosciotti, S. E. Lauro et al. (2022). Automated detection and tracking of hyperbolic diffractions applied to engineering GPR data sets, Proc. 19th Int. Conf. Ground Penetrat. Radar, Soc. Explor. Geophys., 127-130, doi:10.1190/gpr2022-017.1.

Ercoli, M., R. Bizzarri, A. Baldanza, A. Bertinelli et al. (2021). GPR detection of fossil structures in conductive media supported by FDTD modelling and attributes analysis: an example from early pleistocene marine clay at Bargiano site (Central Italy), Geosciences, 11, 9, 386, doi:10.3390/geosciences11090386.

Forte, E., M. Pipan, D. Casabianca, R. Di Cuia et al. (2012). Imaging and characterization of a carbonate hydrocarbon reservoir analogue using GPR attributes, J. Appl. Geophys., 81, 76-87, doi:10.1016/j.jappgeo.2011.09.009.

G1 PA (2021). A Belém, 40% of treated water is wasted due to leaks and illegal connections, https://buff.ly/4gh57GB.

Gamal, M., Q. Di, J. Zhang, C. Fu et al. (2023). Utilizing Ground-Penetrating Radar for Water Leak Detection and Pipe Material Characterization in Environmental Studies: A Case Study, Remote Sens., 15, 20, 4924, doi:10.3390/rs15204924.

Gomes, K. J. M., P. A. C. Oliva, H. O. da Rocha, R. de Alcantara Mendes et al. (2023). Evaluation of the contamination of the subsurface and groundwater by monoaromatic hydrocarbons in an eastern Amazonian town in northern Brazil, Environ. Earth Sci., 82, 1, 23, doi:10.1007/s12665-022-10680-7.

Hong, W. T., S. Kang, S. J. Lee and J. S. Lee (2018). Analyses of GPR signals for characterization of ground conditions in urban areas, J. Appl. Geophys., 152, 65-76, doi:10.1016/j.jappgeo.2018.03.005.

Jol, H. M. (2008). Ground penetrating radar theory and applications, Elsevier, Amsterdam.

Joshaghani, A. and M. Shokrabadi (2022). Ground penetrating radar (GPR) applications in concrete pavements, Int. J. Pavement Eng., 23, 13, 4504-4531, doi:10.1080/10298436.2021.1954182.

Khwanmuang, W. and S. Udphuay (2012). Ground-penetrating radar attribute analysis for visualization of subsurface archaeological structures, Lead. Edge, 31, 8, 946-949, doi:10.1190/tle31080946.1.

Khedaywi, T. and M. Melhem (2024). Effect of Waste Vegetable Oil on Properties of Asphalt Cement and Asphalt Concrete Mixtures: An Overview, Int. J. Pavement Res. Technol., 17, 1, 280-290, doi:10.1007/s42947-022-00234-2.

Klewe, T., C. Strangfeld and S. Kruschwitz (2021). Review of moisture measurements in civil engineering with ground penetrating radar-Applied methods and signal features, Constr. Build. Mater., 278, 122250, doi:10.1016/j.conbuildmat.2021.122250.

Lai, W. W. L., X. Derobert and P. Annan (2018). A review of Ground Penetrating Radar application in civil engineering: A 30-year journey from Locating and Testing to Imaging and Diagnosis, NDT&E INT., 96, 58-78, doi:10.1016/j.ndteint.2017.04.002.

Lai, W. W., R. K. Chang, J. F. Sham and K. Pang (2016). Perturbation mapping of water leak in buried water pipes via laboratory validation experiments with high-frequency ground penetrating radar (GPR), Tunn. Undergr. Space Technol., 52, 157-167, doi:10.1016/j.tust.2015.10.017.

Lambot, S., J. Rhebergen, I. van den Bosch, E. C. Slob et al. (2004). Measuring the Soil Water Content profile of a Sandy Soil with an Off‚ÄêGround Monostatic Ground Penetrating Radar, Vadose Zone J., 3, 4, 1063-1071, doi:10.2136/vzj2004.1063.

Lau, P. K. W., B. W. Y. Cheung, W. W. L. Lai and J. F. C. Sham (2021). Characterizing pipe leakage with a combination of GPR wave velocity algorithms, Tunn. Undergr. Space Technol., 109, 103740, doi:10.1016/j.tust.2020.103740.

Liu, M., Z. Liu, D. Zhou, R. Lan et al. (2020). Recognition method of typical anomalies during karst tunnel construction using GPR attributes and Gaussian processes, Arab. J. Geosci., 13, 16, 1-13, doi:10.1007/s12517-020-05782-0.

Luo, T. X. H. and W. W. L. Lai (2020). GPR pattern recognition of shallow subsurface air voids, Tunn. Undergr. Space Technol., 99, 103355, doi:10.1016/j.tust.2020.103355.

Marfurt, K. J. and T. M. Alves (2015). Pitfalls and limitations in seismic attribute interpretation of tectonic features, Interpretation, 3, 1, SB5-SB15, doi:10.1190/INT-2014-0122.1.

McClymont, A. F., A. G. Green, R. Streich, H. Horstmeyer et al. (2008). Visualization of active faults using geometric attributes of 3D GPR data: An example from the Alpine Fault Zone, New Zealand, Geophysics, 73, 2, B11-B23, doi:10.1190/1.2825408.

Neves, J., A. C. Freire, I. Qamhia, I. L. Al-Qadi et al. (2023). Full-Scale Accelerated Pavement Testing and Instrumentation, in Advances on Testing and Experimentation in Civil Engineering C. Chastre, J. Neves, D. Ribeiro, M. G. Neves et al. (Eds), Springer Tracts in Civil Engineering, Springer, Cham, 163-186, doi:10.1007/978-3-031-05875-2_7.

Nobes, D. C., S. M. Hornblow and J. J. Lapwood (2010). A radar interpretation pitfall: Velocity push-down due to a footwall loess wedge in the ground penetrating radar imaging of the Ostler Fault, New Zealand, SEG Int. Expos. Annu. Meet., doi:10.1190/1.3513226.

Pereira, L. C. C., D. O. Guimarães, M. J. S. Ribeiro and R. M. Costa (2007). Use and occupation in Bragança littoral, Brazilian Amazon, J. Coastal Res., 1116-1120, doi:10.2112/JCR-SI50-202.1.

Raiol, L. L., D. C. R. Santos, K. W. dos Santos Silva, L. P. da Silva et al. (2019). Gerenciamento de pneus inservíveis na cidade de Capanema, Pará, Braz. J. Dev., 5, 12, 30989-31004, doi:10.34117/bjdv5n12-204.

Reis Jr, J. A., D. L. de Castro, T. E. S. de Jesus and F. P. Lima Filho (2014). Characterization of collapsed paleocave systems using GPR attributes, J. Appl. Geophys., 103, 43-56, doi:10.1016/j.jappgeo.2014.01.007.

Reis Júnior, J. A., D. L. de Castro, A. Casas, M. Himi et al. (2015). ERT and GPR survey of collapsed paleocave systems at the western border of the Potiguar Basin in northeast Brazil, Near Surf. Geophys., 13, 4, 369-381, doi:10.3997/1873-0604.2015013.

Riviera, P. P., D. Dalmazzo and E. Santagata (2020). Laboratory Tests for the Characterization of Cold Asphalt Patching Mixtures, in Proceedings of the 9th International Conference on Maintenance and Rehabilitation of Pavements Lecture Notes in Civil Engineering C. Raab (Editor), Springer, Cham, doi:10.1007/978-3-030-48679-2_7.

Rocha, H. O., M. W. C. Silva, F. L. T. Marques and D. C. Leite Filho (2015). Gradiometria magnética e radar de penetração no solo aplicados em Estearias de Penalva (MA), Geol. USP, Sér. Cient., 15, 1, 3-14, doi:10.11606/issn.2316-9095.v15i1p3-14.

Rocha, H., L. Costa and J. Júnior (2016). Investigação geotécnica por meio dos métodos geofísicos SP, Eletrorresistividade e GPR, Geotecnia, 137, 141-155, doi:10.24849/j.geot.2016.137.09.

Rossetti, D. F., F. H. Bezerra and J. M. Dominguez (2013). Late Oligocene-Miocene transgressions along the equatorial and eastern margins of Brazil, Earth Sci. Rev., 123, 87-112, doi:10.1016/j.earscirev.2013.04.005.

Sandmeier, K. J. (1998). Windows™ 7/8/10/11-Program for the processing of seismic, acoustic or electromagnetic reflection, refraction and transmission data, Sandmeier geo. de. Reflexw Software, Karlsruhe, Germany.

Schmalz, B. and B. Lennartz (2002). Analyses of soil water content variations and GPR attribute distributions, J. Hydrol., 267, 3-4, 217-226, doi:10.1016/S0022-1694(02)00152-X.

Switzer, A. D., C. Gouramanis, C. S. Bristow and A. R. Simms (2020). Ground-penetrating radar (GPR) in coastal hazard studies, in Geological Records of Tsunamis and Other Extreme Waves Elsevier, Amsterdam, 8, 143-168, doi:10.1016/B978-0-12-815686-5.00008-0.

Taflove, A. and M. E. Brodwin (1975). Numerical Solution of Steady-State Electromagnetic Scattering Problems Using the Time-Dependent Maxwell's equations, IEEE Trans. Microwave Theory Tech., 23, 8, 623-630, doi:10.1109/TMTT.1975.1128640.

Topp, G. C., J. L. Davis and A. P. Annan (1980). Electromagnetic determination of soil water content: Measurements in coaxial transmission lines, Water Resou. Res., 163, 574-582, doi:10.1029/WR016i003p00574.

Tso, C. H. M., T. C. Johnson, X. Song, X. Chen et al. 2020). Integrated hydrogeophysical modelling and data assimilation for geoelectrical leak detection, J. Contam. Hydrol., 234, 103679, doi:10.1016/j.jconhyd.2020.103679.

Uranga, R. M., G. Manatschal, M. G. Rowan, J. A. Muñoz et al. (2024). Assessing the impact of crustal architecture and along-strike rifting propagation on salt deposition and tectonics: Insights from the Moroccan Atlantic margin, Earth Sci. Rev., 254, 104818, doi:10.1016/j.earscirev.2024.104818.

Van Dam, R. L., J. M. Hendrickx, N. J. Cassidy, R. E. North et al. (2013). Effects of magnetite on high-frequency ground-penetrating radar, Geophysics, 78, 5, H1-H11, doi:10.1190/geo2012-0266.1.

Wang, S. P., H. C. Dan, L. Li, X. Liu et al. (2021). Dynamic response of asphalt pavement under vibration rolling load: Theory and calibration, Soil Dyn. Earthquake Eng., 143, 106633, doi:10.1016/j.soildyn.2021.106633.

Wyllie, M. R. J. and A. R. Gregory (1953). Formation factors of unconsolidated porous media: Influence of particle shape and effect of cementation, J. Pet. Technol., 5, 4, 103-110, doi:10.2118/223-G.

Xiong, X., Y. Tan, J. Hu, X. Hong et al. (2024). Evaluation of Asphalt Pavement Internal Distresses Using Three-Dimensional Ground-Penetrating Radar, International J. Pavement Res. Technol., 1-12, doi:10.1007/s42947-023-00402-y.

Yang, Y., Z. Du, Y. Li, T. Zhang et al. (2022). Anomaly detection of pipeline leakage based on electric field component imaging using ground penetrating radar, Adv. Civ. Eng., 1, 1799750, doi:10.1155/2022/1799750.

Zang, X., Z. D. Xu, H. Lu, C. Zhu et al. (2023). Ultrasonic guided wave techniques and applications in pipeline defect detection: A review, Int. J. Press. Vessels Pip., 105033, doi:10.1016/j.ijpvp.2023.105033.

Zeng, X. and G. A. McMechan (1997). GPR characterization of buried tanks and pipes, Geophysics, 62, 3, 797-806, doi:10.1190/1.1444189.

Zhang, K. and J. Kevern (2021). Review of porous asphalt pavements in cold regions: The state of practice and case study repository in design, construction, and maintenance, J. Infrastruct. Preserv. Resil., 2, 1-17, doi:10.1186/s43065-021-00017-2.

Zhang, W., J. Luo, W. Luo and L. Wang (2024). Leakage diagnostic method for water supply pipeline based on ground penetrating radar and image correlation algorithm, Measurement, 237, 115233, doi:10.1016/j.measurement.2024.115233.

Zhu, H., F. Xiao, Y. Zhou, W. W. L. Lai et al. (2024). A framework for GPR,Äêbased water leakage detection by integrating hydromechanical modelling into electromagnetic modelling, Near Surf. Geophys., Special Issue Ground Penetraining (GPR) Numerical Modelling Research and Practice, 22, 2, 175-187, doi:10.1002/nsg.12281.

***CORRESPONDING AUTHOR: Herson ROCHA**,
UFRJ, IPOLI, Rio de Janeiro, Brazil e-mail: herson.rocha@macae.ufrj.br